Phase behavior and dynamics of fluids in mesoporous glasses

Hyung-June Woo and P. A. Monson
Department of Chemical Engineering, University of Massachusetts, Amherst, Massachusetts 01003
(Received 8 April 2002; revised manuscript received 2 December 2002; published 28 April 2003)

Equilibrium and dynamical relaxation behavior of fluids confined in disordered mesoporous glasses such as Vycor are studied based on a lattice model using mean field theory and Monte Carlo simulations. Preferential attractive interactions between the solid surfaces and the fluid suppresses macroscopic phase separation, while making the relaxation rate increasingly slow. The free energy landscape characterized by the presence of the many metastable minima separated by finite barriers dominates both the static and dynamic behavior of fluids at low temperature. Our results provide additional insight into the nature of hysteresis in adsorption measurements of gases in porous glasses.

DOI: 10.1103/PhysRevE.67.041207 PACS number(s): 61.20.Lc, 61.43.Gt, 64.60.My

I. INTRODUCTION

Confinement of fluids in porous materials can profoundly affect their macroscopic behavior [1]. One important class of materials widely used for various applications is the disordered mesoporous glass, such as Vycor or controlled pore glasses. Typically synthesized via a spinodal decomposition, glassification and subsequent leaching of a binary mixture, disordered mesoporous glasses are characterized by relatively small porosities (volume fraction of void space), mesoscopic length scale of pores, and the disordered, interconnected network of pore structures. Prominent features observed in experiments of gas adsorption in such materials include the apparent absence of the macroscopic phase separation, and widespread hysteresis.

A traditional approach to describing such nontrivial properties is to attempt extensions of the relatively well-known behavior of fluids confined in pores of simple geometries such as slits or cylinders [2]. Detailed descriptions of the static as well as dynamic behavior can be obtained by the density-functional theories and simulations. A rather natural idea of applying such approaches to disordered mesoporous materials is to assume that a macroscopic porous material can be regarded as a collection of independent, noninteracting pores with some statistical distribution of pore sizes. However, the disordered interconnectivity of the adjacent pore regions is ignored in such approaches, excluding the possibility of collective phenomena at length scales exceeding the typical pore size.

An alternative viewpoint is to start from the global, coarse grained picture of the fluid in mesoporous glasses within the statistical mechanical perspective, and consider simple models designed to capture the essential physical ingredients thought to be responsible for the phenomena observed in experiments. The lattice gas, or equivalently the Ising model, provides a natural starting point as a simplified model for the bulk fluids. The disorder that arises from the random spatial distribution of solid matrices, which exerts attractive ''surface fields'' on the the fluid, can be modeled in the simplest level by random fields on each lattice sites, and one arrives at the random field Ising model [3], which has been extensively studied mainly within the context of critical phenomena [4].

The applicability of the random field Ising model in its standard form to fluids in mesoporous glasses with low porosity such as Vycor has often been questioned [5]. Effects of confinement due to the particular structure of the underlying microstructure are ignored entirely. Spatial correlation of the glass solid distribution implies that a second length scale d, namely, the typical domain size of the pore structure, is necessary in addition to the microscopic length scale a of the order of molecular sizes for a minimal description of the system. Nevertheless, some qualitative features observed in the random field Ising model are expected to play important roles for fluids in mesoporous glasses. One of the most important features that arise from the consideration of the random field Ising-type models is the presence of a rugged free energy landscape with many local minima separated by free energy barriers, which dominates thermodynamics at low temperatures.

Recent studies using mean field theory [6,7] of lattice models incorporating the physics of confinement and wetting more realistically in addition to the disorder effects in the random field Ising model have provided useful insights not easily accessible either in detailed molecular simulation studies [8] or studies based on simple pore geometries. They provide a rather natural conceptual explanation of the origin of hysteresis and irreversibility seen in experiments on fluid adsorption in disordered porous materials [6,7]. In the current paper we build on these earlier studies using both Monte Carlo simulations and mean field theory and focusing on a lattice model of a porous glass [6]. We explore the equilibrium behavior in more detail and also study the dynamics of the relaxation processes in the model. Our work yields a fairly comprehensive picture of the equilibrium and dynamic relaxation behavior of fluids in disordered mesoporous glasses.

The lattice model studied in this work is based on a lattice gas with disordered, spatially correlated site dilution and an additional, *nonrandom*, attractive interaction between fluids and solid surfaces [9–11]. It incorporates the main physical elements of confinement, disorder, and wetting in a concise way, and has recently been successfully used to model fluids in porous glasses within the mean field theory [7]. The presence of a very large number of metastable states dominates the global thermodynamic properties, allowing one to capture many of the qualitative features observed in adsorption

experiments within the mean field level.

The paper is organized as follows. Section II describes the model Hamiltonian and its relationship to other models. Section III discusses the Gaussian random field method [7] and its application to the generation of Vycor glass configurations used in the current work. Applications of the mean field theory and Monte Carlo simulations to the adsorption/desorption and equilibrium phase coexistence are discussed in Secs. IV and V, respectively. General aspects of the relaxation behavior of fluids in Vycor, and the conserved order parameter simulation of the lattice model are described in Sec. VI. The final section contains discussion of our results and some concluding remarks. Some of the details of derivations encountered in the above mentioned sections have been collected in the Appendixes.

II. LATTICE MODEL

The lattice model Hamiltonian [9–11] adopted in the current study can be written as

$$\mathcal{H}=-J\sum_{\langle ij\rangle} n_i n_j t_i t_j-\mu\sum_i n_i t_i-yJ\sum_{\langle ij\rangle}[n_i t_i(1-t_j) + n_j t_j(1-t_i)], \tag{1}$$

where $n_i=0,1$ is the usual fluid occupation variable of the lattice gas, and t_i is the quenched random variable representing the solid matrix configuration, equal to either 1 or 0, depending on whether the site i is open to occupancy by the fluid, or blocked by solid, respectively. The double summations run over all of the distinct nearest neighbor site pairs with the fluid-fluid interaction strength J setting the temperature scale of the model, and μ is the chemical potential. The second interaction term in Eq. (1) accounts for the additional attractive interactions between the fluids on the sites next to solid surfaces, whose strength can be varied by adjusting the parameter y. The statistical nature of the quenched disorder $\{t_i\}$ is specified by the probability distribution $P[t_i]$, which can be regarded as a discretized form of the distribution function $P[\rho_s(\mathbf{r})]$ of the solid matrix density field $\rho_s(\mathbf{r})$.

The symmetry of the model as well as its relationship to other models become more apparent in the equivalent Ising form obtained by the transformation into the Ising spin variable, $s_i=2n_i-1$,

$$\mathcal{H}=-\frac{J}{4}\sum_{\langle ij\rangle} s_i s_j t_i t_j-\sum_i h_i s_i t_i, \tag{2a}$$

where irrelevant constant terms have been dropped, and the inhomogeneous field h_i is given by

$$h_i=(\mu+zyJ)/2+\frac{J}{2}(1/2-y)\sum_{j\in i} t_j. \tag{2b}$$

Here z is the coordination number of the lattice, and the sum runs over the nearest neighbors of the site i.

The Ising form (2) shows that the model can be thought of as an Ising model with spatially correlated site dilution, and a "random field" whose distribution is coupled to that of the site dilution via Eq. (2b). The effect of the surface field vanishes and h_i becomes homogeneous when $y=1/2$, and the model reduces to a site diluted Ising model. Many of the nontrivial features manifested by the model arises from the asymmetry $y\neq 1/2$, and it is useful to consider $y-1/2$ as the control parameter responsible for the crossover from the site diluted to the random field type behaviors. However, we emphasize that the model includes the effects of disorder seen in the random field Ising model and the effects of confinement and wetting that are missing in that model.

III. VYCOR GLASS

A. Gaussian random field method

A number of choices for the quenched disorder distribution have been used in the studies of lattice models in the context of the fluids in porous glasses. The simplest choice is to take uncorrelated random distribution of solid sites:

$$P[t_i]=\prod_i [p\,\delta_{t_i,1}+(1-p)\,\delta_{t_i,0}], \tag{3}$$

where p is the porosity.

To incorporate the effects of the second length scale d associated with the pore size of the glasses, it is necessary to add spatial correlations in the solid density distribution $P[t_i]$ [12]. The disordered nature of the solid matrix implies that the porous glass configurations can be efficiently obtained by generating random fields in the three-dimensional space with constraints to their spatial fluctuations designed to match known properties of the material. The uncorrelated random distribution (3) corresponds to the case where the only constraint to the solid density fluctuations is the microscopic cutoff, whose length scale would be of the same order as that of a fluid molecule.

Gaussian random field methods are based on the Cahn model of spinodal decomposition [13], where an auxiliary random field $\phi(\mathbf{r})$ is utilized to generate the physical density of the solid via the level cut,

$$\rho_s(\mathbf{r})=\Theta(\phi(\mathbf{r})-\phi_c), \tag{4}$$

where $\Theta(x)$ is the Heaviside step function. The lattice variable t_i is obtained via the discretization $t_i=1-\rho_s(\mathbf{r}_i)$. The field cutoff ϕ_c, and the spatial correlations of the field can be fixed by the requirement that Eq. (4) correctly yields the statistical properties of the solid density distributions. Similar methods for generating long-range correlations based on the Fourier filtering method have been used by Makse *et al.* [14,15].

For the Vycor glass, prominent characteristics of the material include the porosity $p\simeq 0.3$, and the structure factor $I(q)$ obtained from the small-angle neutron scattering experiments [16]. The porosity controls the average volume fraction of the void spaces, and the structure factor, with its characteristic peak at $q\simeq 0.023$ Å^{-1} [16], reflects the mesoscopic domain structure. The two properties can be directly related to the cutoff ϕ_c and the spatial correlation of the

auxiliary field. A general form of the probability distribution of a Gaussian random field $\phi(\mathbf{r})$ can be written as

$$P[\phi(\mathbf{r})]=\frac{1}{A}\exp\left[-\frac{1}{2}\int\int d\mathbf{r}d\mathbf{r}'\,\phi(\mathbf{r})G^{-1}(|\mathbf{r}-\mathbf{r}'|)\phi(\mathbf{r}')\right], \tag{5}$$

where $G(r)$ is the two-point correlation function of the random field defined as

$$G(r)=\langle\phi(0)\phi(\mathbf{r})\rangle, \tag{6}$$

in which $r=|\mathbf{r}|$, the brackets denote the average with respect to the probability distribution,

$$\langle\cdots\rangle\equiv\int\mathcal{D}\phi P[\phi(\mathbf{r})](\cdots), \tag{7}$$

and A is the normalization constant in Eq. (5). Since the amplitude of the auxiliary field is arbitrary, we set $G(0)=\langle\phi(\mathbf{r})^2\rangle=1$. The constraints can be written as

$$1-p=\langle\rho_s(\mathbf{r})\rangle, \tag{8a}$$

$$I(q)\propto\hat{M}(q), \tag{8b}$$

where $\hat{M}(q)$ is the Fourier transform of the solid density correlation function $M(r)=\langle\rho_s(0)\rho_s(\mathbf{r})\rangle-p^2$. Using Gaussian functional integrals, it can be shown that the relations can be explicitly written as [18]

$$1-p=\frac{1}{2}\mathrm{erfc}(\phi_c/\sqrt{2}), \tag{9a}$$

$$M(r)=p(1-p)-\frac{1}{2\pi}\int_{G(r)}^{1}\frac{dt}{\sqrt{1-t^2}}e^{-\phi_c^2/(1+t)}. \tag{9b}$$

Figures 1 and 2 show the correlation functions of the physical density $\rho_s(\mathbf{r})$ and the auxiliary field $\phi(\mathbf{r})$ in Fourier space and real space, respectively. The solid density distribution can be obtained by generating sets of random complex numbers $\hat{\phi}(q)$ with zero mean and variance $\langle|\hat{\phi}(\mathbf{q})|^2\rangle=\hat{G}(q)$ subject to the constraint

$$\hat{\phi}(\mathbf{q})^*=\hat{\phi}(-\mathbf{q}) \tag{10}$$

on a cubic lattice with lattice spacing a, such that $L=Na$. Fourier inversion is then performed with the fast Fourier transform [19]. Due to the errors arising from discretization, filtering the resulting field $\phi_{\mathbf{r}}$ at the cutoff ϕ_c given by Eq. (9a) does not give the accurate porosity p originally intended. We instead adjusted the cutoff value for each realizations such that the level cut yields the porosity $p=0.3$.

Figures 3 and 4 show the solid surface visualized by interpolations of the level cut, Eq. (4), and the two-dimensional cross sections on the lattice for two different choices of the lattice constant $a=30$ Å and $a=15$ Å. The face centered cubic (fcc) lattice has been used throughout the work described here. The solid density field obtained by the level cut of the Gaussian random field on the cubic lattice with spacing a was imported into an fcc lattice with the cubic lattice constant $b=2a$.

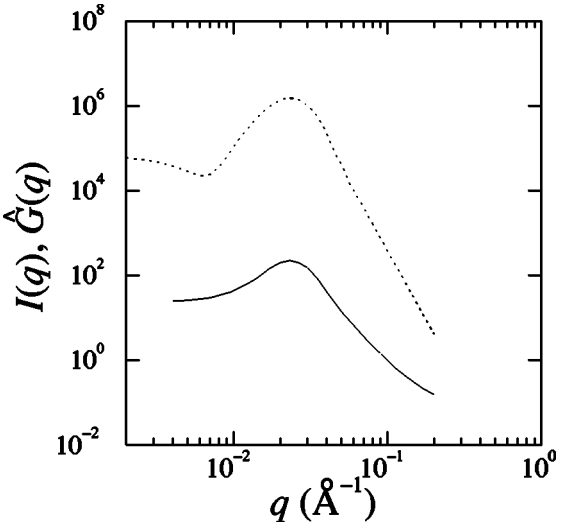

FIG. 1. Structure factor of Vycor $I(k)$ (solid line, in units of cm^{-1}) from Ref. [17], and the correlation function of the Gaussian auxiliary field in Fourier space, $\hat{G}(q)$ (dotted line), calculated by Eqs. (9) with $p=0.3$.

The parameter a sets the scale of resolution of the method, with smaller values yielding better description of the microscopic structure of the pores, whereas the overall computational costs would be largely determined by the number of cubic unit cells along each dimension N. For physical samples of fixed linear dimension $L=Na$, better microscopic resolutions achieved by smaller a values require more computational costs. Although a values affect the overall behavior of the system quantitatively, qualitative behaviors were found to be similar with different choices. Systems with $a=30$ Å were used for most of the calculations reported, with comparisons with $a=15$ Å case in Secs. IV and V. Unless otherwise noted, system sizes were $N=32$ and $N=16$ for the mean field and Monte Carlo simulations, with results

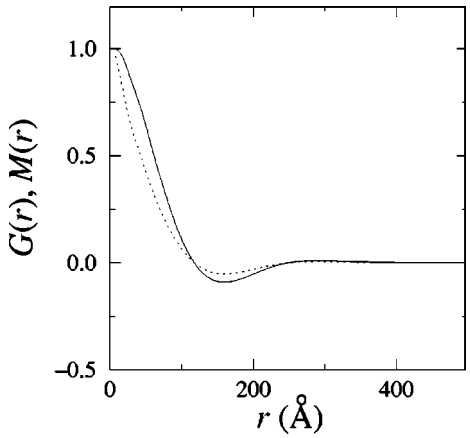

FIG. 2. Real space correlation functions of the physical density $M(r)/p(1-p)$ (solid line) and the auxiliary field $G(r)$ (dotted line).

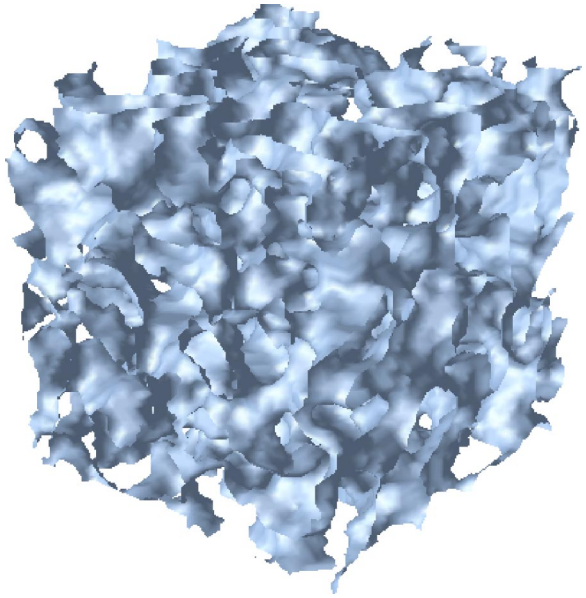

FIG. 3. Solid surfaces generated by the Gaussian random field method. The linear dimension of the cubic box corresponds to $L = N_c a = 960$ Å, where $N_c = 64$ is the number of lattice grids used for each dimension, and $a = 15$ Å is the lattice spacing.

averaged over more than 10 disorder samples. We do not consider critical properties of the model in this paper, and the size of the system used in the Monte Carlo simulations is expected to have little effect on the qualitative behavior as long as it is considerably larger than the typical pore sizes.

B. Percolation properties

An important requirement for a realistic model of the Vycor glass matrix is the bicontinuity of the pore and solid regions throughout the three-dimensional space. Depending on the spatial correlations of the pore space, there generally exists a percolation threshold as the porosity is increased, below which most of the pores are statistically disconnected, preventing fluid adsorption throughout the material.

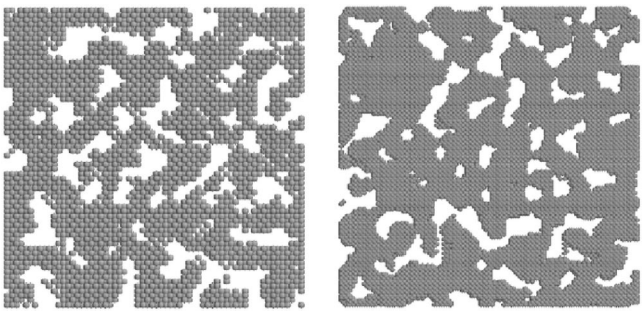

FIG. 4. Two-dimensional cross sections of the lattice variable configurations $\{t_i\}$ on fcc lattice, with spheres representing the sites where $t_i = 0$ (solid). The left- and right-hand side images were generated with $a = 30$ Å, $N = 32$, and $a = 15$ Å, $N = 64$, respectively, where $2a$ and N are the size and number of the cubic unit cell along each dimension. The physical length of the box is $L = 1920$ Å in both cases.

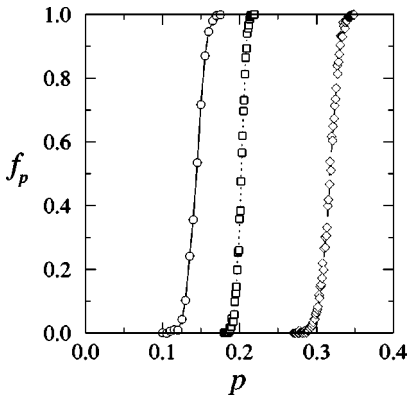

FIG. 5. Percolation probability as a function of the porosity p. Diamonds and rectangles are for the uncorrelated random distribution on the simple cubic and fcc lattices, respectively. Circles are for the Vycor glass distribution generated by the Gaussian random field method with $a = 30$ Å. Systems with $N = 32$ were used in all cases. Symbols represent the fraction of percolating realizations among 500 disorder samples.

A convenient measure of the percolation property is provided by $f_p(p)$, the fraction of the disorder realizations in which there exists at least one path starting from a site within one face of the lattice ($x = 0$) and reaching the other face ($x = L$). The paths are allowed only on sites for which $t_i = 1$. For a given lattice with a set of disorder realizations $\{t_i\}$, $f_p(p)$ can be easily calculated by initializing spins in the voids as $s_i = -1$ for a given realization, growing clusters from the sites at $x = 0$ by recursively visiting all neighboring sites with $t_j = 1$ and $s_j = -1$ as in the Wolff cluster algorithm for the Monte Carlo simulation [20,21], while unconditionally flipping spins within the cluster. A realization is identified as percolated when the other face is reached at any time, whereas if all possible paths have been searched without reaching the other end, the realization is identified as nonpercolated. The probability $f_p(p)$ is obtained by calculating the fraction of percolated realizations within the ensemble of the total disorder realizations.

The percolation threshold p_c is defined as the value of the porosity where the probability f_p makes a discontinuous jump in the thermodynamic limit. Threshold values have been determined for a variety of lattices [22] for the uncorrelated site disorder, Eq. (3). The value for the simple cubic lattice is $p_c \simeq 0.31$, indicating that the pores in the simple cubic, uncorrelated random matrix at the porosity of Vycor do not percolate the space well. Higher coordination number facilitates percolations, and $p_c \simeq 0.20$ for the random matrix on fcc lattice. Figure 5 shows the percolation probability $f_p(p)$ calculated for the random and Vycor glass matrices on the cubic and fcc lattices. The presence of spatial correlations significantly lower the percolation threshold, and the porosity $p = 0.3$ is well above the threshold for the Vycor glass configurations generated by the Gaussian random field method.

IV. MEAN FIELD THEORY

Mean field theory provides important qualitative insights for Ising-like lattice models, especially for disordered sys-

tems. We first consider the symmetric case, $y=1/2$, for which the Ising form of the model, Eq. (2a), is more convenience. The free energy F is given by the quenched average

$$F=\langle F[t_i]\rangle_t, \tag{11}$$

where $\langle\cdots\rangle_t \equiv \Sigma_{\{t_i\}}(\cdots)P[t_i]$ and

$$e^{-\beta F[t_i]} \equiv Z[t_i]=\sum_{\{s_i\}} e^{-\beta\mathcal{H}}, \tag{12}$$

in which $\beta=1/k_BT$ as usual. A generalized form of the mean field theory [23] (Appendix A) gives

$$Z[t_i]=\sum_{\alpha} e^{-\beta F_\alpha}, \tag{13}$$

where

$$\beta F_\alpha=\sum_i \left[\frac{1+m_i^\alpha}{2}\ln\frac{1+m_i^\alpha}{2}+\frac{1-m_i^\alpha}{2}\ln\frac{1-m_i^\alpha}{2}\right] - \frac{\beta J}{4}\sum_{\langle ij\rangle} m_i^\alpha m_j^\alpha-\sum_i \beta h_i m_i^\alpha \tag{14}$$

is the free energy of the minimum α, satisfying the mean field equation

$$m_i^\alpha=t_i\tanh\left[(\beta J/4)\sum_{j\in i} m_j^\alpha+\beta h_i\right]. \tag{15}$$

For a pure system such as the Ising model, there usually exist one or two minima of Eq. (14), corresponding to the high temperature or broken symmetry phases. In contrast, in the disordered systems such as the current model, the mean field equation potentially possesses a large number of metastable minima, which are represented by the index α. Expressions for the macroscopic observables directly follow from the free energy (14). In particular, the average magnetization (density in the fluid language) is given by $m=-\langle\partial F[t_i]/\partial h_i\rangle_t=\langle m_i\rangle_t$, where

$$m_i=\frac{\sum_\alpha m_i^\alpha e^{-\beta F_\alpha}}{\sum_\alpha e^{-\beta F_\alpha}}. \tag{16}$$

The local mean field equation (15) can be solved numerically on the lattice with a given realization of the disorder $\{t_i\}$ by starting with an initial guess of $\{m_i^\alpha\}$ and iterating until convergence is achieved. Different solutions are obtained depending on the initial condition of the iteration.

For the symmetric case $y=1/2$, the model reduces to the site diluted Ising model, where it has been well established that the phase transition persists for the disorder realizations that percolate the space [24]. The dilution lowers the critical temperature T_c which approaches zero at the percolation threshold.

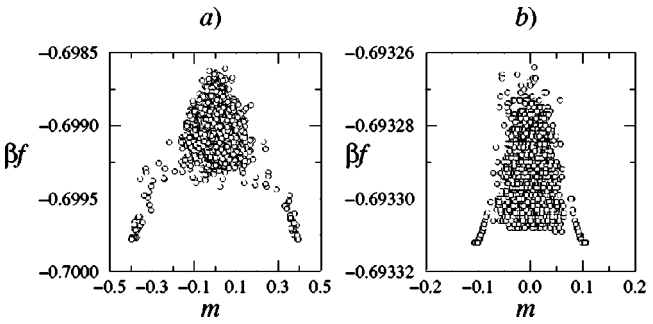

FIG. 6. Distributions of the mean field free energy minima near the critical point for $y=0.5$ with $a=15$ Å; (a) $T^*=0.8$, (b) $T^*=0.9$.

To search for multiple minima, the initial conditions of iteration were chosen by randomly assigning magnetizations by Gaussian distributions around various mean and variances, which were also chosen randomly. Below the critical point $T^*<T_c^*$, where $T^*=T/T_{cb}$ is the reduced temperature defined with respect to the bulk critical point T_{cb}, the solutions are enveloped by the ''maximal solutions'' [23], whose magnetization has the largest magnitude, and are the two global minima of the distribution. At temperatures away from the critical point, the free energy difference between the maximal solutions and the rest of the minima is large, causing expression (13) to be dominated by the term corresponding to the maximal solution. As we approach the critical region, the free energy difference becomes smaller, and the contributions from the other solutions increase (Fig. 6).

To calculate the equilibrium magnetization from Eq. (16) below the critical point, the summation over the minima found needs to be partitioned into two phases. For $y=1/2$, the symmetry naturally dictates the partitioning into $m_\alpha>0$ and $m_\alpha<0$. The average magnetization curve calculated by Eq. (16) near the critical point is shown in Fig. 7, along with that of the maximal solution. An exhaustive search for the minima even for a moderately sized lattice would be a daunting task, and the weighted average shown in Fig. 7 includes only a part of the nonmaximal solutions. The residual magnetizations near the critical point, similar to the finite size

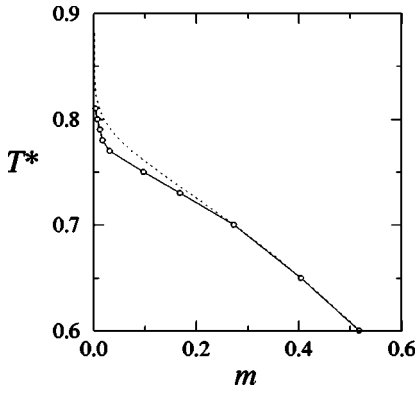

FIG. 7. Average magnetization versus temperature for $y=1/2$ and $a=30$ Å. A single sample with $N=32$ was used. Circles connected by the solid line are the weighted average calculated by Eq. (16), and the dotted line corresponds to the maximal solutions.

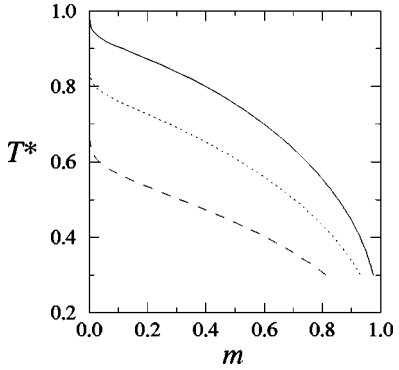

FIG. 8. Loci of maximal solutions for $y=1/2$ for $a=15$ Å (solid line), $a=30$ Å (dotted line), and $a=50$ Å (dashed line).

effects typically seen in Monte Carlo simulations, result from the incompleteness of the numerical solution search that underestimates the contributions of the nonmaximal solutions to the weighted average.

Although the numerical search for the set of local free energy minima described above cannot be expected to be complete even for small systems, it can uncover important qualitative differences in the free energy landscape of the system for different conditions. From Fig. 6, for example, one can expect that in the thermodynamic limit, the system properties could either be dominated by the few minima, or be influenced by the presence of rugged landscape characterized by minima whose number increases exponentially with system sizes. A systematic study of the number of solutions with increasing system size would be helpful, although such a study would necessarily be limited to very small systems, for which the quality of statistics for the glass representations would be rather poor.

The location of the critical point T_c^* depends on the relative degree to which the void space is percolated, and therefore on the parameter a, which determines the typical pore size in units of the lattice constant. As $a\rightarrow 0$, each pore reduces to the bulk fluid, and $T_c^*\rightarrow 1$. Figure 8 shows the maximal solution boundary for three different values of a. The effect of confinement for $a\lesssim 10$ Å is seen to be small for the symmetric site diluted model in the Vycor glass matrix. The qualitative trend of the critical temperature as a function of the effective domain size d/a in units of the lattice constant agrees with the previous study of the site diluted Ising model on Vycor-like glass matrices using Monte Carlo simulations [25].

The Ising symmetry no longer exists when $y>1/2$, and it is more convenient to use the lattice gas form of the model. The mean field equation analogous to Eqs. (14) and (15) for the grand potential functional reads

$$\beta\Omega_{\alpha}=\sum_i\ [\rho_i^{\alpha}\ln\rho_i^{\alpha}+(1-\rho_i^{\alpha})\ln(1-\rho_i^{\alpha})]-\beta\mu\sum_i\ \rho_i^{\alpha}$$

$$-\beta J\sum_{\langle ij\rangle}\ [\rho_i^{\alpha}\rho_j^{\alpha}+y\rho_i^{\alpha}(1-t_j)+y\rho_j^{\alpha}(1-t_i)], \quad (17)$$

where the density $\rho_i^{\alpha}=\Sigma_{\{n_i\}}n_i t_i e^{-\beta\mathcal{H}}$ satisfies

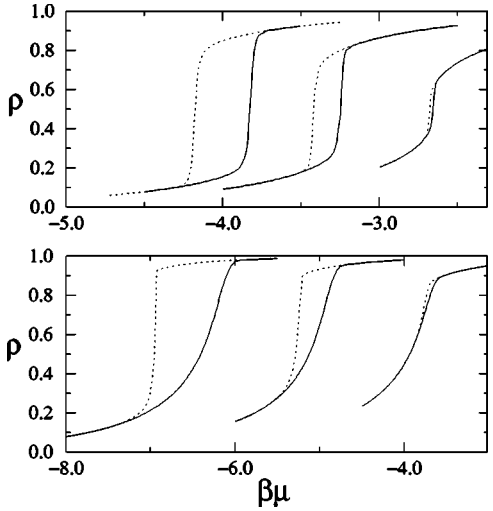

FIG. 9. Mean field adsorption (solid lines) and desorption (dotted lines) isotherms ρ for $y=0.5$ (top) and $y=1.0$ (bottom). From the left to right, $T^*=0.5$, 0.6, and 0.75 for $y=0.5$ and $T^*=0.4$, 0.5, and 0.65 for $y=1.0$, respectively.

$$\rho_i^{\alpha}=\frac{t_i}{1+\exp\left[-\beta\mu-\beta J\sum_{j\in i}\ (\rho_j^{\alpha}+y-yt_j)\right]}. \quad (18)$$

Using Eq. (18), the locus of maximal solutions for a given temperature is easily found by numerical iterations. We start with $\mu\simeq\pm\infty$ and change the value of μ in either directions by small increments, while determining the average density

$$\rho=\left\langle\frac{1}{N_s}\sum_i\ \rho_i^{\alpha}\right\rangle_t, \quad (19)$$

where N_s is the total number of sites with $t_i=1$, for each chemical potential values via numerical iterations [6,7]. The previous set of local density values satisfying the mean field equation is used as the initial guess for iteration for the next value of chemical potential. This locus corresponds to the adsorption isotherms of fluids measured in experiments. The change in chemical potential as the control parameter induces the transitions between neighboring local free energy minima. Figure 9 shows a typical set of adsorption isotherms for $y=0.5$ and $y=1.0$. For the symmetric case, the hysteresis gap retains much of the typical behavior seen in the pure systems, an exception being the smoothing (due to disorder) of the discontinuous jump in density around the spinodal of pure systems.

As we turn on the surface fields by increasing y from $y=1/2$, the hysteresis region develops the characteristic asymmetry seen in experiments of fluid adsorption in mesoporous glasses. Whereas the adsorption branch remains smooth, the desorption branch shows a precipitous drop in density in a narrow range of chemical potentials, which tends to become more pronounced as y increases and temperature decreases. In contrast to the symmetric case, the mean field free energy minima were found to show broader distributions (Fig. 10), and the maximal solutions no longer dominate.

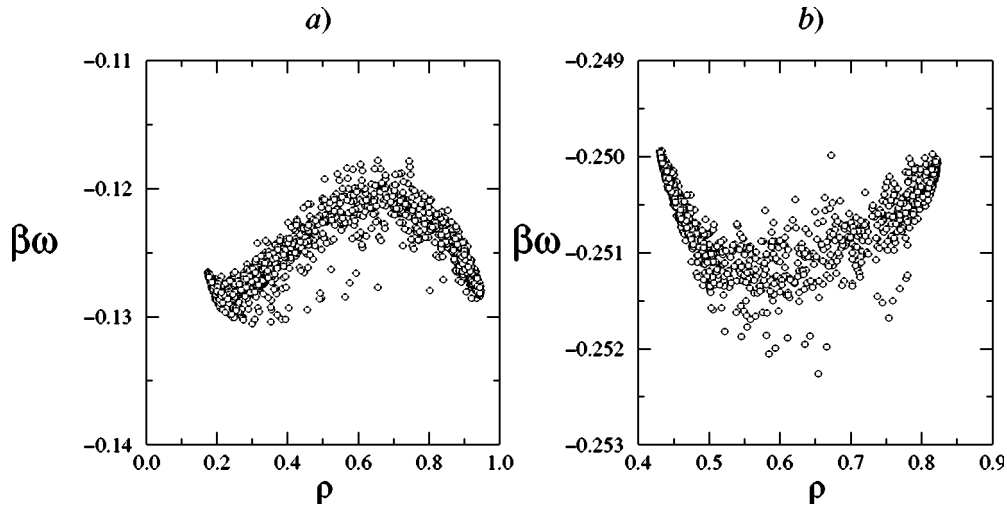

FIG. 10. Distributions of the mean field free energy minima near coexistence for $y=0.7$ below and above the critical point; (a) $T^*=0.4$, $\beta\mu=-5.623$ and (b) $T^*=0.6$, $\beta\mu=-3.687$.

The interior of the hysteresis region shown in Fig. 9 contains many local minima of the mean field free energy (the number of minima would be essentially inifinite in the thermodynamic limit), revealed by the myriad of intermediate solutions to the mean field equation found when we traverse the control parameter μ space in various directions, producing the so-called ''scanning curves'' [7]. The gradual crossover from the conventional two-phase coexistence of bulk fluids with the free energy characterized by the two minima separated by a barrier proportional to the interfacial free energy, to the strongly hysteretic behavior due to the large multiplicity local minima is expected to occur as we increase y from the symmetric value. For the case of $y=1/2$, the free energy barriers between local minima would mainly be due to the entropic factors associated with the disordered arrangement of confining blockers, and therefore relatively small. Little qualitative difference is expected in the noncritical phase behavior compared to the pure system limit, except the depression of the subcritical phase separations to lower temperature regimes.

As the field is turned on ($y>1/2$), the barriers would increase due to the attractive interactions between solid surfaces and the fluid inside the pores, developing the local ruggedness of the free energy landscape. The increasing free energy barriers and the resultant hysteresis appears superimposed to the global bimodal feature of the free energy, which in turn becomes eventually overshadowed by the field effects, and for strong fields the two-phase coexistence normally encountered in bulk fluids is expected to be largely irrelevant. Such qualitative behavior is also observed in the random field Ising model, where there exists a critical field strength above which no phase transition exists [26,27].

To confirm such trends of the equilibrium phase coexistence within the mean field theory, the hysteresis region was first identified by calculating the locus of maximal solutions (adsorption/desorption isotherms) as in Fig. 9, and the distributions of the free energy minima were searched for a number of chemical potential values inside the hysteresis region. At sufficiently low temperatures, the distribution shows the bimodal character near coexistence (Fig. 10). The summation in Eq. (16) was partitioned into two ''phases'' for which $\rho_\alpha<\rho_c$ and $\rho_\alpha>\rho_c$, respectively. The critical density ρ_c, initially guessed, can be refined to achieve the overall consistency of the coexistence curve. The grand free energy of phase i is defined as

$$\Omega^{(i)}=-k_BT\ln\left[\sum_{\alpha\in \mathrm{i}} e^{-\beta\Omega_\alpha}\right], \tag{20}$$

where the sum is over all local minima of the grand potential associated with phase i. At coexistence the grand free energies of the two phases are equal. The corresponding phase densities are given by

$$\rho^{(i)}=e^{\beta\Omega^{(i)}}\sum_{\alpha\in i}\rho_\alpha e^{-\beta\Omega_\alpha}. \tag{21}$$

Approximate phase coexistence densities for various values of y are shown in Fig. 11. Shown together are the boundaries of the hysteresis region, the two densities at which the hysteresis gap opens and closes. For the site diluted case $y=0.5$, the hysteresis boundary remains close to the coexistence curve, and as one lowers the temperature, the onset of hysteresis occurs near the critical point, a feature commonly observed in pure systems.

As the surface field increases, the global two-phase coexistence is suppressed to lower temperatures, whereas the temperature regime where hysteresis begins to develop remains nearly independent of y. Hysteresis and equilibrium phase coexistence develop at two distinct temperatures T_h and T_c, respectively. In the temperature regime $T_c<T<T_h$, the free energy landscape is dominated by multiplicity of local minima without any macroscopic phase separation. The nontrivial symmetry breaking characterized by the appearance of rugged free energy landscape at T_h is analogous to the replica symmetry breaking transition observed in the models of spin glasses [28]. As the Thouless-Anderson-Palmer approach for spin glasses, the local mean field theory

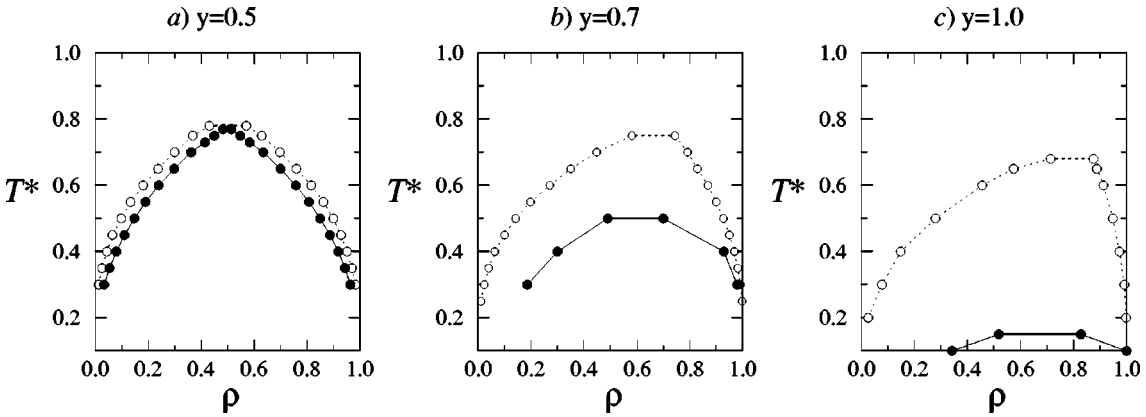

FIG. 11. Mean field phase coexistence densities (filled circles, solid lines) and the boundaries of hysteresis region (open circles, dotted lines) for three different values of y. Lines are guides to the eye.

adopted to the present model readily reveals the signatures of the rugged free energy landscape.

Although the first-order phase transition and the two-phase coexistence characterized by the bimodal free energy retains its global feature at lower temperatures for $y>1/2$, each of the many free energy minima shown in Fig. 10 are separated by finite free energy barriers. The probability of crossing these local barriers and ultimately achieving the global equilibrium by phase separating into two phases indicated by the coexistence conditions in Fig. 11 would become exponentially small as temperature decreases. Therefore, it is expected that the equilibrium phase transitions shown to persist for $y>1/2$ in Fig. 11 would be largely unattainable, and therefore practically irrelevant in experimental situations.

V. MONTE CARLO SIMULATION

The fact that the local mean field method captures many of the phenomenologies observed in experiments, such as hysteresis and scanning behavior [6,7], suggests that thermal fluctuations, ignored in the mean field theory, generally are in fact not strong enough to allow efficient barrier crossings in experimental time scales. Monte Carlo simulations of the model can provide a more quantitative understanding of the effect of fluctuations, or equivalently, typical barrier heights in the free energy landscape. Extensive Monte Carlo simulation studies have been performed for the random field Ising model, mainly focused on the study of critical phenomena [4,25,27]. Viewed in terms of the lattice gas representation of the current model, such simulations correspond to the lattice analog of the grand canonical simulations of molecular models, in which thermal equilibrium is sought by creating and destroying molecules with a specified chemical potential.

The presence of the rugged free energy landscape and the resultant glassiness typically pose formidable challenges to achieving equilibration in Monte Carlo simulations [21]. A variety of algorithms [21,27,29] have been developed to facilitate local barrier crossings, while still enforcing ergodicity and detailed balance, and efficiently simulate disordered systems. We limit our scope in this section to two issues. We show that such a dramatic slow down of the dynamics also occurs in the current model as the surface field is turned on, and investigate the accuracy of the qualitative trend of equilibrium phase behavior observed in the mean field analyses for small $y-1/2$.

As in the mean field theory, $y=1/2$ case of the model can be studied by a straightforward application of the methods for pure systems. The cluster update algorithm due to Wolff [20] efficiently eliminates critical slowing down, and can be applied to the site diluted case by allowing cluster growth only on the vacant sites [25]. Due to the Ising symmetry, the simulation samples two phases connected by spin flip symmetry with equal probability below T_c^*, and coexistence densities away from the critical point can be easily obtained by calculating the average of the magnitude,

$$\rho^{(1)}=\frac{\langle|m_i|\rangle+1}{2}, \quad \rho^{(2)}=1-\rho^{(1)}, \tag{22}$$

where the brackets represent the thermal average.

In addition, we consider the generalized free energy $\beta f(\rho)$ for a given sample $\{t_i\}$ defined as

$$\exp[-N_s\beta f(\rho)]=\sum_{\{n_i\}}\delta\left(\frac{1}{N_s}\sum_i n_i t_i-\rho\right)e^{-\beta H}. \tag{23}$$

For a pure system, the free energy $\beta f(\rho)$ as a function of the order parameter corresponds to the Landau-type free energy, which changes its shape into bimodal form as we lower the temperature across the critical point. In simulations, it can be calculated by collecting histograms of density values for a number of discretized bins, and taking the logarithm of the distribution. Figure 12 shows the free energy $\beta f(\rho)$ near the critical point for the symmetric case, $y=0.5$. For the disordered cases, the generalized free energy, as the projection of the full free energy functional into the bulk density plane, can serve as an analog of the mean field counterpart shown in Fig. 10. It allows one to locate first-order phase transitions, if any, in the absence of the Ising symmetry.

We again proceed to the asymmetric case by considering the adsorption/desorption isotherms. Local free energy barriers encountered in relaxations responsible for the slow dynamics observed in experiments also severely impede equilibration of the single spin flip (and to a lesser extent,

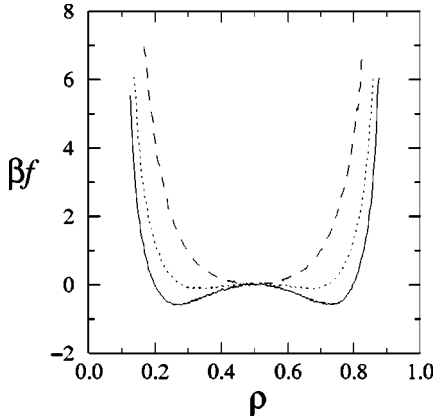

FIG. 12. Free energy as a function of density near the critical point for $y=0.5$ from Monte Carlo simulations. Solid, dotted, and dashed lines are for $T^*=0.52$, $T^*=0.53$, and $T^*=0.55$, respectively, where $T^*=T/T_{cb}$ is the reduced temperature with respect to the bulk critical point $T_{cb}=2.449J/k_B$ [30]. The absolute values of the free energy have been shifted such that $\beta f=0$ for $\rho=0.5$.

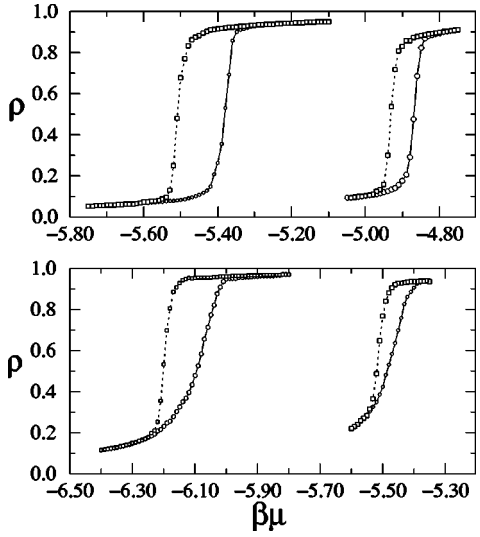

FIG. 13. Adsorption/desorption isotherms from Metropolis Monte Carlo simulations with $\tau_h=500$ GMCS. $y=0.5$, and 0.7 for the top and bottom panels, and $T^*=0.45$, and 0.5, from left to right.

cluster update) Monte Carlo simulations. Noncritical slowing down of equilibration in the Metropolis algorithm thus closely reflects the glassiness in real dynamics associated with fluid adsorption, and the hysteresis region can be located by identifying regions where the equilibration is unusually slow. A more quantitative dynamical interpretation of the relaxation in terms of Monte Carlo simulations is discussed in Sec. VI.

In pure systems, the relaxation time of the Metropolis simulation diverges with a power law near the critical point, whereas it remains relatively small in the noncritical regimes. Mean field analyses discussed in the preceding section suggest that for the present model, as the field strength is increased, signatures of the ubiquitous free energy barriers would appear as widespread slowing down of relaxations away from the critical point. Such onset of nontrivial hysteresis in fact occurs via a gradual crossover within a range of temperatures. The analog of the hysteresis boundaries from the Monte Carlo simulations can thus be obtained by scanning chemical potential values gradually in either directions as in mean field theory, but only allowing equilibrations for a relatively short time period τ_h. The time scale τ_h, given in terms of the spin flip attempts per sites or Glauber Monte Carlo steps (GMCS), would have to be larger than relaxation times of noncritical pure systems, while small enough such that barrier crossings, if any, would not occur appreciably. Figure 13 shows the Monte Carlo analog of the sorption isotherms for $y=0.5$, and $y=0.7$, where the equilibration time was taken as $\tau_h=500$ GMCS.

The qualitative trends observed in adsorption isotherms obtained by Monte Carlo simulations closely follow those within the mean field theory. However, the boundaries of the hysteresis region are less clear cut than in mean field theory, and the onset of the nontrivial hysteresis due to the multiple free energy minima occurs within a range of the parameter space without any sharp transition. Approximate hysteresis boundaries are shown in Fig. 15 for symmetric and weakly asymmetric cases. For $y=0.5$, strong thermal fluctuations produce hysteresis near the critical region, whereas turning on the surface field would effectively quench thermal fluctuations. The hysteresis observed for $y>0.5$ would be mainly due to the presence of local free energy barriers rather than critical slowing down.

To uncover the fate of the first-order phase transition of the $y=1/2$ case as one turns on the surface field, we calculate the grand potential per site $\beta\omega(\rho)$ at a number of chemical potential values within the hysteretic regime. The presence of surface fields, and the resulting local barriers significantly impede equilibrations of the Monte Carlo simulations even for small $y-1/2$, and a straightforward calculation of the free energy as in Fig. 12 becomes difficult. We get around the difficulty by performing the umbrella sampling [31]. The density range is divided into a number of windows of width $\delta\rho$, and simulations collecting histograms are performed within each window $\rho_n<\rho<\rho_n+\delta\rho$ via a non-Boltzmann sampling such that any move that puts the system outside the window is rejected [32]. Pieces of the free energy curve from each window are combined together by shifting the absolute values such that the free energy becomes continuous at the window boundaries. At coexistence, the two minima obtained would be equal in free energy values. Given an initial guess of the coexistence chemical potential, reweighting of the free energy can be used to locate the coexistence condition via

$$\beta\omega(\rho;\mu')=\beta\omega(\rho;\mu)-\sum_n \beta(\mu'-\mu)\rho_n+\text{const.} \tag{24}$$

Figure 14 shows the free energy near coexistence for $y=0.6$ and $y=0.7$. By comparing the free energy profiles for the two cases, we observe that increasing the surface field introduces local ''ruggedness'' into the landscape, which gradually overshadows the global bimodal character of the

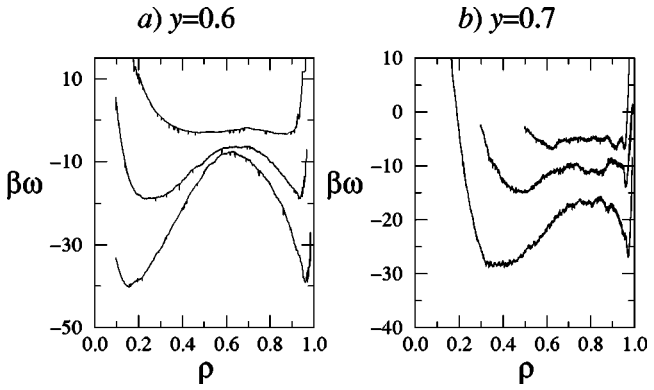

FIG. 14. Grand potential landscape near coexistence for $y=0.6$ and $y=0.7$. Temperature and chemical potential values are $(T^*,\beta\mu)=(0.4,-6.5285)$, $(0.45,-5.791)$, $(0.5,-5.1953)$ for $y=0.6$, and $(0.4,-6.903)$, $(0.43,-6.4065)$, $(0.45,-6.108)$ for $y=0.7$ from the bottom to the top. The absolute values of the free energy are arbitrary.

two-phase coexistence, while lowering the critical temperature. Coexistence densities located as the two minima of the free energy in Fig. 14 are shown in Fig. 15. Although the slow equilibration of the simulation does not allow one to go further into higher values of $y-1/2$, the qualitative behavior closely agrees with the mean field results shown in Fig. 11.

The relative ''smearing'' of the transition temperature T_h in simulations compared to the mean field case indicates that the glassiness develops within a range of temperatures rather than via a sharp transition, and barrier crossings do happen within the crossover regime. However, the probability for crossings would become exponentially small as temperature is lowered away from the crossover, and the equilibration needed to achieve macroscopic phase separations is expected to be unavailable for $y\gtrsim 0.7$. Similar situation is also observed in spin glasses, where the mean field theory with infinite range interactions predicts the spin glass transition temperature below which free energy barriers between minima become infinite in the thermodynamic limit, whereas such idealization is thought to be only partially reflected in short ranged models [28].

VI. DYNAMICS OF RELAXATION

A. Nonconserved dynamics

The disappearance of the two-phase coexistence as the field strength is increased, as shown in Fig. 15, implies that for fluids in mesoporous glasses, thermodynamic driving force for macroscopic phase separation vanishes. Therefore, the properties of adsorption and desorption of fluids into a porous glass sample in contact with gas reservoirs, rather than phase separation dynamics of fluids that has been often studied in relation to porous materials [33–35], become more relevant. In this section, we consider the dynamical aspects of the density relaxation in a more quantitative fashion with Monte Carlo simulations.

The standard Metropolis algorithm for the Monte Carlo simulations can be regarded as an implementation of a particular dynamical model of Markovian stochastic processes, which yields realizations of the nonequilibrium average of the density

$$\overline{\rho_i}(t)=\sum_{\{n_i\}} n_i P_m[n_i;t] \tag{25}$$

measured in units of GMCS such that $\tau_0=1$ GMCS, where $P_m(n_1,\ldots,n_N;t)$ is the probability of $n_i(t)$. A coarse grained version of the stochastic dissipative dynamics in or near equilibrium can be described by the Langevin-type equation (model *A*) [36]

$$\frac{\partial}{\partial t}\rho(\mathbf{r},t)=\chi\tau_0^{-1}\left[-\frac{\delta\beta F}{\delta\rho}+\eta(\mathbf{r},t)\right], \tag{26}$$

where $\chi=\partial\rho/\partial\beta\mu$ is the compressibility, F is the Landau-Ginzburg-type free energy functional of the form of Eq. (14), and $\eta(\mathbf{r},t)$ is the stochastic random force assumed to be Markovian:

$$\langle\eta(\mathbf{r},t)\rangle=0,\quad \langle\eta(\mathbf{r},t)\,\eta(\mathbf{r}',t')\rangle=\frac{2\tau_0}{\chi}\delta(\mathbf{r}-\mathbf{r}')\,\delta(t-t'). \tag{27}$$

Glauber dynamics or model *A* (26) provide qualitative descriptions of the nonconserved order parameter relaxation

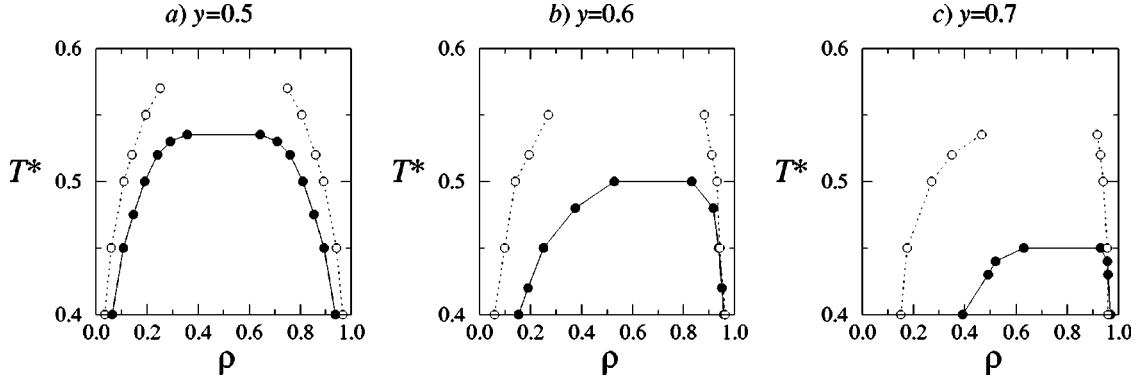

FIG. 15. Phase diagrams from Monte Carlo simulations. Filled and open circles are the coexistence densities, and the approximate boundaries of hysteresis region, respectively. Lines are guides to the eye.

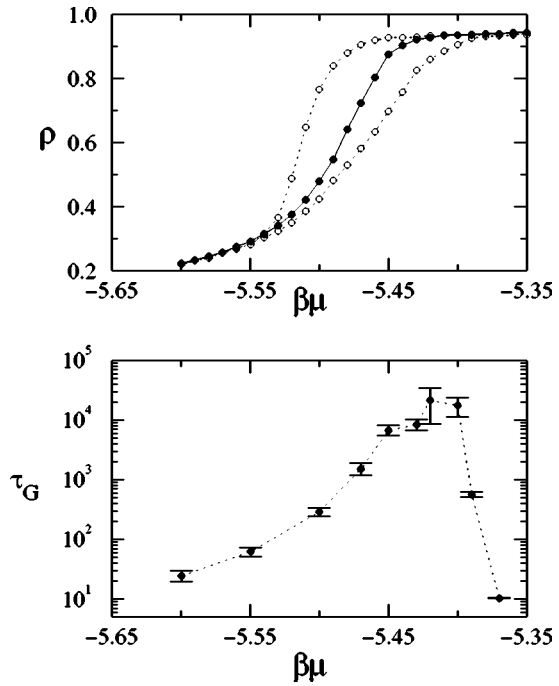

FIG. 16. Density relaxations in Glauber dynamics for $y=0.7$ and $T^*=0.5$. The top panel shows the adsorption and desorption isotherms (open symbols connected by dotted lines) obtained with $\tau_h=500$ GMCS, and the equilibrium isotherm (filled circles with solid lines). The bottom panel shows the integrated relaxation time obtained from the time correlation function.

dynamics near equilibrium in systems such as random field Ising spins or spin glasses. For fluids in porous materials, the relaxation rate obtained can be regarded as a lower bound to the actual rate since mass conservation, in general, further restricts density relaxations. In particular, it is expected that the strongly hysteretic regimes as shown in Fig. 13 where Glauber dynamics show unusually slow relaxation rates, would be paralleled in the conserved case with even slower rates.

Nonconserved order parameter dynamics of the random field Ising model shows behavior qualitatively different from the ordinary critical dynamics of pure systems. The presence of random fields, while pinning down thermal fluctuations, create local free energy barriers, and changes the usual power law scaling of the relaxation time into the Arrhenius-type activated dynamics [37]

$$\tau_G \sim \exp[A(\xi/a)^{\psi}], \tag{28}$$

where ξ is the correlation length and ψ is a dynamical exponent. The exponential dependence of the relaxation time on temperature in Eq. (28) provides a natural conceptual explanation of the glassy dynamics and hysteresis seen in experiments on fluids in disordered pores, and is consistent with the presence of a large number of local minima in the free energy landscape revealed by the mean field treatment.

To examine the nonconserved dynamics of the model, we consider the hysteretic regime above the first-order phase transition for $y=0.7$ and $T^*=0.5$, shown in Fig. 16. As seen in Fig. 15, the condition corresponds to the region where the

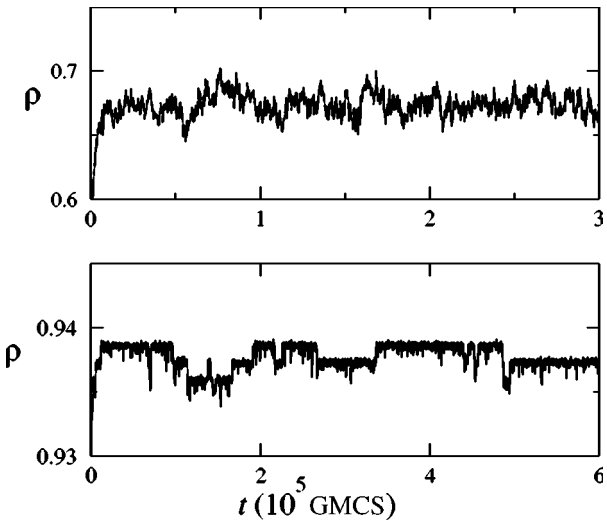

FIG. 17. Density fluctuations at equilibrium in Glauber dynamics for $y=0.7$ and $T^*=0.5$ at $\beta\mu=-5.47$ (top), and $\beta\mu=-5.4$ (bottom).

crossover into the strongly hysteretic regime begins to happen for a relatively small $y-1/2$, allowing us to achieve equilibrium with the conventional Wolff algorithm (shown as filled circles in Fig. 16) and examine the onset of activated dynamics and glassiness with relative ease.

Since the equilibrium conditions are known, a well-defined measure of the relaxation rate is provided by examining the time correlation function of density fluctuations around the equilibrium value. Typical density time series for two different conditions along the equilibrium isotherm are shown in Fig. 17. The activated nature of the density fluctuations is clearly seen, which becomes more pronounced for higher densities, where the system is typically stuck in a local minimum of free energy for relatively long time periods and makes infrequent transitions to neighboring minima made possible by occasional barrier crossings.

The evolution of the relaxation time of Glauber dynamics τ_G, defined as the integrated autocorrelation time of the density correlation function calculated from the time series is shown in Fig. 16. It is seen that the relaxation time increases exponentially as one gets inside the hysteresis region. The slowing down of Glauber dynamics is due to the increasing role that the activated barrier crossing plays in equilibration, not to an underlying second-order phase transition as one usually encounters in pure systems. The hysteresis one observes in adsorption experiments is accordingly due to the presence of multitudes of free energy minima arising from the disorder, and the system's inability to cross the local barriers within the experimentally realizable time scale, rather than the ''conventional'' type of hysteresis and first-order phase transition, as has often been assumed previously, where two free energy minima corresponding to the low and high density phases compete with a barrier between them proportional to the interfacial contribution.

B. Conserved dynamics

As discussed in the preceding section, Glauber dynamics does not conserve mass, and therefore only provides indirect

guidance on real dynamics of fluid adsorption in porous glasses. Huse has considered the effect of order parameter conservation to the activated dynamics of the random field Ising model [38]. It was argued that there exists a crossover wave vector that distinguishes the diffusion limited and the activated dynamics regime. In terms of the dynamic structure factor for a wave vector corresponding to length scales larger than the typical pore sizes, one initially observes a fast exponential decay of correlations due to diffusion as in normal fluids, followed by a slow and stretched residual component that corresponds to the activated dynamics between local minima in free energy landscape [39]. The latter regime is characterized by a broad distribution of relaxation times in logarithmic scale, consistent with the activated dynamics picture, Eq. (28).

The presence of the dynamical crossover between the initial diffusion-limited regime and the subsequent activation dominated regime provides a natural explanation for the phenomenology observed in typical adsorption experiments of fluids [40], where one encounters relatively rapid relaxations of the fluid density in response to a change in external control parameters such as vapor pressure of the gas reservoir, followed by a ''quasiequilibrium'' stage where the system remains essentially unchanged over periods of time many orders of magnitude longer than the initial time scale. To describe such relaxation behavior with the current model, we consider in this section a quantitative connection between the nonconserved Glauber dynamics and conserved dynamics of fluids.

The analog of model *A* equation (26) that includes mass conservation law is the model *B* [36] equation, which can be written in **q** space as

$$\frac{\partial \rho_{\mathbf{q}}}{\partial t} = -D\chi q^2[\beta\hat{\mu}[\rho_{\mathbf{q}}] + \eta_{\mathbf{q}}(t)], \tag{29}$$

where D is the diffusion coefficient, and $\hat{\mu}$ is the Fourier transform of $\mu[\rho]=\delta F/\delta\rho(\mathbf{r},t)$. The random field is characterized by

$$\langle \eta_{\mathbf{q}}(t)\rangle = 0,$$

$$\langle \eta_{\mathbf{q}}(t)\,\eta_{-\mathbf{q}'}(t')\rangle = \frac{2}{D\chi q^2}\,\delta_{\mathbf{q},\mathbf{q}'}\,\delta(t-t'). \tag{30}$$

The mass conservation law, reflected by the presence of the q^2 factor ($-\nabla^2$ in the real space) in Eqs. (29) and (30), would significantly slow down the already slow glassy relaxations of nonconserved dynamics of the model, and it would be useful to be able to estimate the time scales of conserved dynamics from Glauber dynamics simulations. In fact, comparing Eqs. (26), (27), and (29), (30), we note that a **q**-dependent time rescaling

$$\bar{t}_{\mathbf{q}} = Dq^2 t_0 t \tag{31}$$

puts the model *B* equations into an effective model *A* form. The density elements $\{\rho_{\mathbf{q}}(t)\}$ in Eq. (29) are coupled to one another via the nonlinear functional $\hat{\mu}$ generating nontrivial behaviors such as glassy dynamics. Once obtained, each component represents the time evolution of the average density of a volume element with linear dimension $L=2\pi/q$ with respect to the uniform time scale t. By renormalizing the physical time scale with Eq. (31), which amounts to a contraction, the equation of motion satisfied by the original solution is transformed into Eqs. (26) and (27) with t replaced by $\bar{t}_{\mathbf{q}}$.

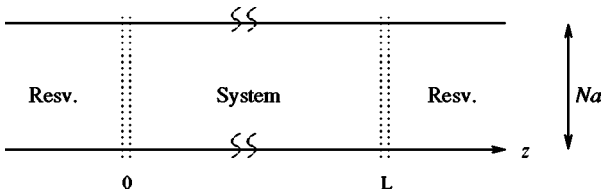

FIG. 18. Kawasaki dynamics simulation setup. Both the reservoir and the system are filled with a realization of the porous glass. Periodic boundary conditions apply to the x and y directions. Fluids in the reservoirs and in the system are simulated by Glauber and Kawasaki dynamics, respectively. The interfaces at $z=0$ and $z=L$ are updated by both algorithms.

Physically, the rescaling factor

$$\tau_D = \frac{L^2}{4\pi^2 D} \tag{32}$$

in Eq. (31) corresponds to the diffusive relaxation time of the volume element needed to produce an elementary fluctuation in the bulk density with mass conservation. By contracting the time scale into a unit of τ_D, we are ''relaxing'' the conservation law and treating the system in an effective grand canonical ensemble. In practice, Eq. (31) allows one to estimate the conserved dynamics from simulations of nonconserved dynamics, which are less demanding in general. As a special case, one expects that the characteristic relaxation time of conserved dynamics, τ_K, can be estimated by

$$\tau_K = \tau_D \tau_G / t_0. \tag{33}$$

C. Kawasaki dynamics simulation

A general quantity that can be examined to study the conserved order parameter dynamics of fluid density is the dynamical structure factor $\langle \rho_{-\mathbf{q}}(0)\rho_{\mathbf{q}}(t)\rangle$ measured in light scattering experiments. However, to calculate the structure factor for a wave vector **q** with conservation law from simulations, it is necessary to consider a system much larger than $L=2\pi/q$, such that appreciable density fluctuations become possible in the volume element of size L with the rest of the volume serving as the reservoir.

We instead choose to mimic a typical situation in adsorption experiments [41], depicted in Fig. 18, where a system with linear dimension L is in contact with grand canonical reservoirs at $z=0$ and $z=L$ kept at a chemical potential, and probe the time dependent response of the density inside the system reacting to a sudden change in the external control parameter. Periodic boundary conditions are used for x and y directions, reducing the spatial variations into one dimen-

sion. A realization of Vycor glass spans both the system and reservoirs, whereas fluids in the system and reservoirs evolve with Kawasaki and Glauber dynamics, respectively. Similar techniques have been used by Leung and Luzar [42] in the study of water cavitation dynamics in slit geometry of hydrophobic surfaces.

In the simulation, one MCS (Monte Carlo step) first consists of a random selection of a fluid particle inside the system, and attempting to move it into one of its vacant neighboring sites, which are repeated N_v times where N_v is the total number of particles inside. It is followed by the Glauber step, in which a void site in the reservoirs are chosen for updating N_s times, where N_s is the total number of sites with $t_i=1$ in the reservoirs. Care must be taken in the treatment of the interfacial regions at $z=0$ and $z=L$ not to introduce any artificial bias into the dynamics of the total system. The two-dimensional planes of interfacial regions were separated from the rest, and as the third step of the MCS, sites with $t_i=1$ were chosen at random within the planes, Glauber updating was attempted, and when it resulted in $n_i=1$, a subsequent diffusion attempt was made. In addition, the diffusive moves of fluid particles inside the system into the boundary planes were followed by Glauber updates.

To initiate relaxation dynamics, the system and the reservoirs are first equilibrated with Glauber dynamics, each at two different chemical potentials such that the initial uniform density profiles at ρ_0 and ρ_∞, respectively, for the system and the reservoirs are obtained. Time is set as $t=0$ and the total system evolves via the composite algorithm described above. The dynamical relaxation is probed by measuring the one-dimensional density profile,

$$\overline{\rho}(z,t)=\frac{\rho(z,t)-\rho_0}{\rho_\infty-\rho_0}, \tag{34}$$

with $\overline{\rho}(z,0)=0$ and $\overline{\rho}(z,\infty)=1$. If one assumes that the dynamics is entirely described by the simple diffusion with diffusion coefficient D, one can obtain the solution to the diffusion equation as (Appendix B)

$$\overline{\rho}(z,t)=1-4\sum_{n=1,3,5,\ldots}^{\infty}\frac{\sin\dfrac{n\pi z}{L}}{n\pi}e^{-D(n\pi/L)^2t}. \tag{35}$$

The average density inside the system $\overline{\rho}(t)=\int_0^L(dz/L)\overline{\rho}(z,t)$ is given by

$$\overline{\rho}(t)=1-8\sum_{n=1,3,5,\ldots}\frac{e^{-D(n\pi/L)^2t}}{n^2\pi^2}. \tag{36}$$

The small t limit of the solution is (Appendix B)

$$\overline{\rho}(z)\simeq 4\left(\frac{Dt}{\pi L^2}\right)^{1/2}. \tag{37}$$

The $t^{1/2}$ scaling of Eq. (37) can in fact be inferred from the dimensional argument [43]. The prefactor of the initial scaling regime given by Eq. (37) allows one to extract values of the diffusion coefficient of fluids in Vycor from simulations.

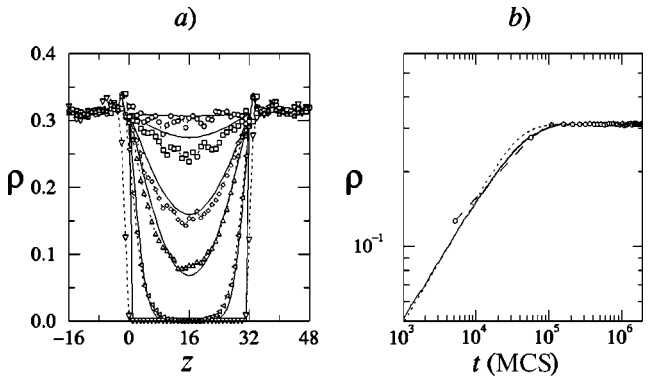

FIG. 19. (a) Time evolution of density profile for $y=0.7$, $T^*=0.8$, $\beta\mu=-3.6$, $\rho_0=0$, $\rho_\infty=0.31$. The z coordinate shown is in units of $b=2a$. Symbols and solid lines are the Kawasaki dynamics simulation and the ideal diffusion profile at $t=1$, 1×10^3, 1×10^4, 2×10^4, 5×10^4, and 1×10^5 in MCS, respectively. $D=5\times10^{-3}$ b^2/MCS. (b) Bulk density in the Kawasaki dynamics (solid line), ideal diffusion [Eq. (36); dotted line], and the Glauber dynamics rescaled by τ_D/t_0 with $t_0=1$ GMCS.

We first consider a typical behavior away from the hysteretic regime, where a normal fluidlike behavior is expected. With a single minimum dominating the free energy landscape, density relaxations would be essentially diffusion limited, described well by the ideal diffusion result, Eq. (35). Figure 19 shows the time evolution of the density profile inside the system as well as the bulk density for a nonequilibrium relaxation at $y=0.7$, $T^*=0.8$, and $\beta\mu=-3.6$, where no appreciable hysteresis is found in grand canonical simulations. The relaxation behavior closely agrees with the prediction of the ideal diffusion with the diffusion coefficient D obtained by the initial straight line portion of the logarithmic plot of $\overline{\rho}(t)$, which corresponds to Eq. (37). Also shown in Fig. 19 is the Glauber dynamics density relaxation, rescaled by the diffusional relaxation time τ_D, which agrees well with the Kawasaki dynamics results. It corresponds to Eq. (33) with $\tau_G\sim O(1)$ GMCS.

Figure 20 shows the corresponding results at a lower temperature at $y=0.7$, $T^*=0.5$, and $\beta\mu=-5.55$, which is located at a boundary of the hysteresis region shown in Fig. 16. The initial diffusion limited regime with $t^{1/2}$ scaling ends around $t\simeq\mathcal{O}(10^4)$ MCS, and the bulk density relaxation makes a crossover in logarithmic scale into the effective grand canonical relaxation represented by the Glauber dynamics rescaled by τ_D.

The bulk density relaxations shown in Figs. 19 and 20 are expected to have similar behavior when probed in terms of the dynamic structure factor measured in scattering experiments. The $t^{1/2}$ scaling, and the effective Glauber dynamics relaxation regimes correspond to the standard exponential decay of correlations due to diffusion, and the stretched relaxations with broad distribution of time scales of the correlation function.

Close agreement of the effective Glauber dynamics rescaled by the diffusive relaxation time with the conserved

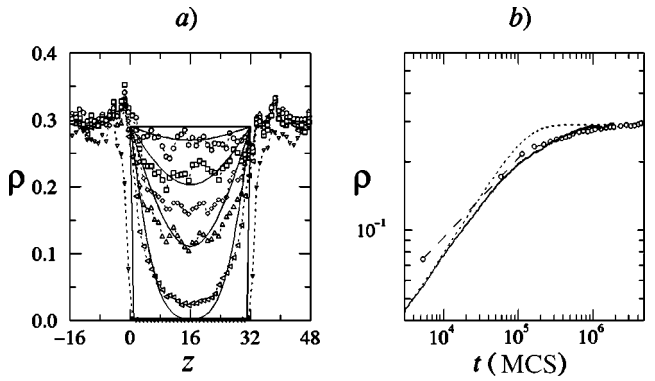

FIG. 20. (a) Time evolution of density profile for $y=0.7$, $T^*=0.5$, $\beta\mu=-5.55$, $\rho_0=0$, $\rho_\infty=0.31$. Symbols and solid lines are the Kawasaki dynamics simulation and the ideal diffusion profile at $t=1$, 1×10^3, 1×10^4, 2×10^4, 5×10^4, and 1×10^5 in MCS, respectively. $D=1.5\times10^{-3}\ b^2$/MCS. (b) Bulk density as a function of time. Symbols are the same as in Fig. 19 with $\tau_0=0.31$ GMCS.

dynamics allows one to estimate τ_K via Eq. (33) for situations where the slow glassy dynamics due to the activated barrier crossings prohibits one to perform conserved order parameter simulations for large systems. The relaxation time τ_G in a noncritical system is nearly independent of the system size, and a fairly good estimate can be made with simulations of a moderately sized system. An additional estimate of the diffusion coefficient D for the system from sources such as the $t^{1/2}$ scaling regime in Fig. 20 yields τ_K for samples of arbitrarily large sizes.

One can calibrate Kawasaki dynamics of the pure lattice gas to make connections from the simulation time scale in units of the Monte Carlo steps (MCS) per site to the physical time scale [42]. Figure 21 shows the diffusion coefficient of the bulk lattice gas on an fcc lattice obtained by calculating the cumulative mean square displacements of a tagged particle at $T^*=0.55$, which roughly corresponds to the triple point temperature of argon. Comparing the diffusion coefficients of argon at the triple point $D=1.6\times10^{-5}$ cm^2 s^{-1} [44] and that of the lattice gas near the high density limit $D\simeq0.005\ a^2$MCS^{-1}, we get 1 MCS$\simeq$0.03 ns for $a=30$ Å. With $\tau_G\sim\mathcal{O}(10^2)$ MCS for the simulated system of Fig. 20, $\tau_K/L^2\sim\mathcal{O}(10^5)$ s cm^{-2}. Diffusion coefficient is found to decrease significantly as density increases. An analogous simulation of the initial diffusion limited regime yielded $D\simeq2.0\times10^{-5}b^2$/MCS for $\beta\mu\simeq-5.45$ and $\rho_0=0.4$, which corresponds to the condition deep inside the hysteresis region in Fig. 20, where $\tau_G\sim\mathcal{O}(10^4)$ GMCS. Equation (33) gives $\tau_K/L^2\gtrsim\mathcal{O}(10)$ yr/cm^2.

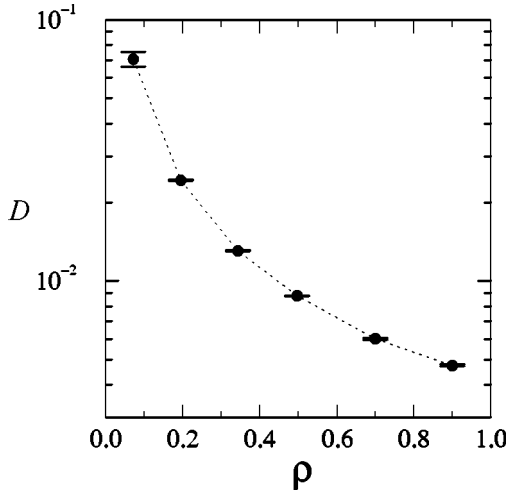

FIG. 21. Self-diffusion coefficient of the bulk lattice gas at $T^*=0.55$ as a function of density. D is in units of a^2/MCS.

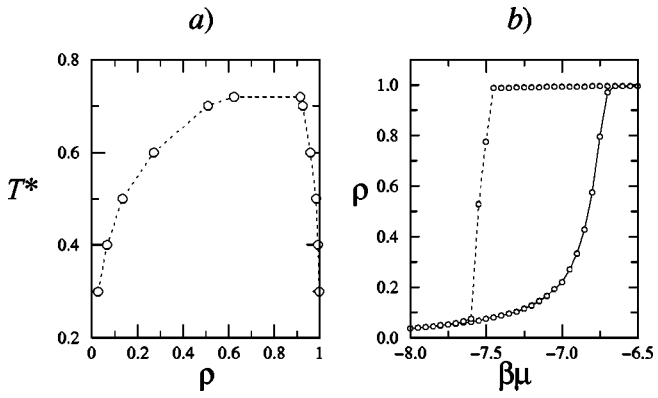

FIG. 22. (a) Boundaries of hysteresis region and (b) adsorption/desorption isotherms for $a=15$ Å, $y=0.9$ from the Monte Carlo simulations. $T^*=0.4$ in (b).

The overall dynamics as well as relaxation times would be a function of the lattice constant a among other parameters. The value $a=30$ Å chosen for the simulations described above is expected to overestimate the degree to which barrier crossings occur in density relaxations. Since a filled pore contains approximately $\sim(d/a)^3$ lattice sites, each of which acting as a single particle in Monte Carlo simulations, a collective motion of the group of particles filling a pore would become more likely as a increases. As a is decreased to microscopic lengths ~5 Å corresponding to the molecular size of adsorbing gases, barrier crossings would become increasingly improbable, and the relaxation times would, in general, be longer than those obtained for the Hamiltonian with larger values of a.

As a partial confirmation of such trend, we examine the relaxation in the Glauber dynamics in the hysteretic regime for $a=15$ Å at $T^*=0.4$ (Fig. 22). A few typical trajectories in the Glauber dynamics starting with different initial conditions are shown in Fig. 23. Long periods of quasiequilibrium in local minima are punctuated with rare fluctuations corresponding to the barrier crossings. The overall relaxation time is expected to be $\tau_G\gtrsim\mathcal{O}(10^6)$. Assuming that the diffusion coefficient is smaller than the value found for conditions in Fig. 20, each of the typical quasiequilibrium stages shown in Fig. 23 would have durations of the order of more than several years/cm^2.

VII. CONCLUSION

The mean field and Monte Carlo simulation results described in this paper provide a fairly comprehensive under-

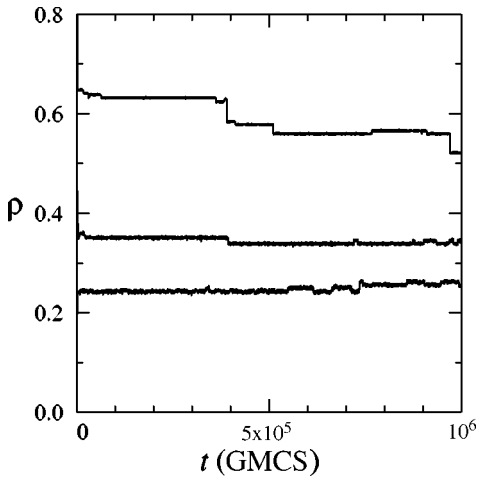

FIG. 23. Density relaxations in Glauber dynamics for $a=15$ Å, $y=0.9$, and $T^*=0.4$ with various initial conditions.

standing of the phenomenologies observed in experiments of fluid adsorption on disordered mesoporous glasses. The thermodynamic behavior is fundamentally changed by the appearance of the large number of local free energy minima as the asymmetry parameter $y-1/2$ is increased from zero. The local mean field theory provides a natural platform to study such qualitative features, and gives an accurate qualitative description of the hysteretic and scanning behavior found in adsorption/desorption experiments [6,7]. The effects of thermal fluctuations allowing the system to cross local free energy barriers are expected to be minimal, in general, under conditions appropriate for real fluids (large field, $y-1/2$), as indicated by the trends obtained in our Monte Carlo simulations.

In adsorption experiments, one typically observes that a change in external vapor pressure is followed by a fairly rapid approach to a quasiequilibrium state, which subsequently appears unchanged over experimentally accessible time periods [40]. The latter dynamical regime has often been confused as corresponding to the *thermodynamic* metastable phase one encounters in the conventional first-order phase transition as in pure systems and wetting transitions. The two stage nature of the density relaxations described in Sec. VI, consisting of the diffusion limited and the activated dynamics regimes, provides a natural and direct explanation of such phenomenology.

It will be of interest to see whether one can use off-lattice models that incorporate molecular properties of adsorbing gases as well as fluid-solid interactions more faithfully, and make more detailed quantitative predictions based on the overall picture described within the current model. Another important aspect that has not been treated here is the effect of hydrodynamic flows on the dynamics. Inclusion of momentum conservation to the dynamical equations such as Eq. (29) and related implementations of the coarse grained simulation based on the current model might provide valuable insights.

ACKNOWLEDGMENT

This work was supported by the National Science Foundation (Grant Nos. CTS-9906794 and CTS-0220835).

APPENDIX A: MEAN-FIELD THEORY

We consider the Ising Hamiltonian, Eq. (2a), with an extra external field δh_i,

$$\mathcal{H}=-\frac{1}{2}\sum_{ij} J_{ij}s_it_is_jt_j-\sum_i h_i's_it_i, \tag{A1}$$

where $h_i'=h_i+\delta h_i$ and $J_{ij}=(J/2)\,\delta_{|\mathbf{r}_i-\mathbf{r}_j|,a}$. The free energy is given by

$$-\beta F=\langle \ln Z[t_i]\rangle_t, \tag{A2}$$

where

$$Z[t_i]=\sum_{\{s_i\}} e^{-\beta\mathcal{H}}. \tag{A3}$$

The average magnetization, assumed to be self-averaging, is given by $m=\langle m_i\rangle_t$, where m_i is the thermal average for a given sample,

$$m_i=\frac{\partial \ln Z[t_i]}{\partial\beta\,\delta h_i}. \tag{A4}$$

Applying the Hubbard-Stratonovich transformation to $Z[t_i]$ [45] gives

$$Z[t_i]=\sum_{\{s_i\}}\int \mathcal{D}\psi \exp\Bigg[-\frac{1}{2}\sum_{ij}\psi_iK_{ij}\psi_j+\sum_i [s_it_i(\psi_i+\beta h_i')]\Bigg], \tag{A5}$$

where $\mathcal{D}\psi$ includes the normalization factor. The interaction matrix K_{ij} for the field is related to the spin interaction by $K_{ij}=k_BTJ_{ij}^{-1}$. Summing over $\{s_i\}$, we get

$$Z[t_i]=\int \mathcal{D}\psi e^{-S[\psi_i,t_i]}, \tag{A6}$$

where the action is given by

$$S[\psi_i,t_i]=\frac{1}{2}\sum_{ij}\psi_iK_{ij}\psi_j-\sum_i \ln 2\cosh[t_i(\psi_i+\beta h_i')]$$
$$=\frac{1}{2}\sum_{ij}\psi_iK_{ij}\psi_j-\sum_i t_i\ln 2\cosh(\psi_i+\beta h_i'), \tag{A7}$$

in which the constant term has been dropped in the second line.

Mean field profiles $\{\overline{\psi}_i^{\alpha}\}$ satisfy the equation $\partial S/\partial\psi_i|_{\overline{\psi}_j^{\alpha}}=0$ or

$$\sum_j K_{ij}\overline{\psi}_j^{\alpha}=t_i\tanh(\overline{\psi}_i^{\alpha}+\beta h_i'). \tag{A8}$$

The solution index α allows for the situations where there exist many distinct solutions to Eq. (A8), characteristic of the disordered systems. The mean field approximation amounts to including contributions to the functional integral in Eq. (A6) only from the minima:

$$\overline{Z}[t_i]=\sum_{\alpha} e^{-S[\overline{\psi}_i^{\alpha},t_i]}. \tag{A9}$$

Equation (A4) becomes

$$m_i=\frac{1}{\overline{Z}[t_i]}\sum_{\alpha} m_i^{\alpha}e^{-S_{\alpha}}, \tag{A10}$$

where

$$m_i^{\alpha}=-\frac{\partial S_{\alpha}}{\partial\beta\delta h_i}=t_i\tanh(\overline{\psi}_i^{\alpha}+\beta h_i') \tag{A11}$$

and $S_{\alpha}\equiv S[\overline{\psi}_i^{\alpha},t_i]$. The minimized action S_{α}, given in terms of the field $\overline{\psi}_i^{\alpha}$, can be replaced by the Legendre transform in the zero-field limit,

$$\beta F_{\alpha}[m_i^{\alpha}]=\lim_{\delta h_i\to 0}\left[S_{\alpha}+\sum_i \beta\delta h_i m_i^{\alpha}\right]. \tag{A12}$$

Equations (A7), (A8), (A11), and (A12) yield Eqs. (14) and (15).

APPENDIX B: IDEAL DIFFUSION

We consider the ideal one-dimensional diffusion of fluids with diffusion coefficient D in the system shown in Fig. 18. The density profile at time t, $\rho(z,t)$ satisfies the diffusion equation

$$\frac{\partial\rho}{\partial t}=D\frac{\partial^2\rho}{\partial z^2} \tag{B1}$$

subject to the boundary and initial conditions

$$\rho(0,t)=\rho(L,t)=\rho_{\infty}, \tag{B2a}$$

$$\rho(z,0)=\rho_0 \quad (0<z<L). \tag{B2b}$$

In the asymptotic limit $L\to\infty$, or $t\to 0$, the couping between the two interfaces at $z=0$ and $z=L$ can be ignored, and the solution can be written as

$$\rho(z,t)\simeq\rho_i(z,t)+\rho_i(L-z,t), \tag{B3}$$

where $\rho_i(z,t)$ is the profile for the system bounded with an interface only at $z=0$. The calculation of $\rho_i(z,t)$ is most easily done by exploiting the symmetry at $z=0$ [43], which yields

$$\rho_i(z,t)=\rho_0+\Delta\rho\left[1-\mathrm{erf}\left(\frac{z}{2\sqrt{Dt}}\right)\right], \tag{B4}$$

where $\Delta\rho=\rho_{\infty}-\rho_0$. The reduced density $\overline{\rho}(z,t)=[\rho(z,t)-\rho_0]/\Delta\rho$ is given by

$$\overline{\rho}(z,t)\simeq 2-\mathrm{erf}\left(\frac{z}{2\sqrt{Dt}}\right)-\mathrm{erf}\left(\frac{L-z}{2\sqrt{Dt}}\right), \tag{B5}$$

which is valid for $L\gg 2\sqrt{Dt}$. The average inside the system $\overline{\rho}(t)=(1/L)\int_0^L dz\,\overline{\rho}(z,t)$ corresponding to Eq. (B5) is

$$\overline{\rho}(t)\simeq 2\left[1-\mathrm{erf}\left(\frac{L}{2\sqrt{Dt}}\right)-2\left(\frac{Dt}{\pi L^2}\right)^{1/2}(e^{-L^2/4Dt}-1)\right]. \tag{B6}$$

Taking the limit $Dt/L^2\to 0$ of Eq. (B6) yields Eq. (37).

For large t with a finite L, fluids inside the system is affected by both of the interfaces, producing deviations from Eqs. (B5) and (B6). To find the general solution, we expand $\overline{\rho}(z,t)$ in Fourier series [46] as

$$\overline{\rho}(z,t)=\left(\frac{2}{L}\right)^{1/2}\sum_{n=1}^{\infty} a_n(t)\sin\frac{n\pi z}{L}, \tag{B7}$$

such that it satisfies the boundary condition $\overline{\rho}(0,t)=\overline{\rho}(L,t)=0$. Substitution into Eq. (B1) yields the equation for the Fourier coefficient,

$$\frac{da_n}{dt}=\frac{2^{1/2}n\pi D}{L^{3/2}}[1-(-1)^n]-D(n\pi/L)^2a_n(t). \tag{B8}$$

The initial condition (B2b) implies $a_n(0)=0$. Solving Eq. (B8), we get

$$a_n(t)=\frac{(2L)^{1/2}}{n\pi}[1-(-1)^n][1-e^{-D(n\pi/L)^2t}]. \tag{B9}$$

Substitution of Eq. (B9) into Eq. (B7) gives Eq. (35).

[1] L.D. Gelb, K.E. Gubbins, R. Radhakrishnan, and M. Sliwinska-Bartkowiak, Rep. Prog. Phys. **62**, 1573 (1999).
[2] R. Evans, J. Phys.: Condens. Matter **2**, 8989 (1990).
[3] P.-G. de Gennes, J. Phys. Chem. **88**, 6469 (1984).
[4] D.P. Belanger and A.P. Young, J. Magn. Magn. Mater. **100**, 272 (1991).
[5] L. Monette, A.J. Liu, and G.S. Grest, Phys. Rev. A **46**, 7664 (1992).
[6] E. Kierlik, P.A. Monson, M.L. Rosinberg, L. Sarkisov, and G. Tarjus, Phys. Rev. Lett. **87**, 055701 (2001).
[7] H.-J. Woo, L. Sarkisov, and P.A. Monson, Langmuir **17**, 7472 (2001).
[8] L.D. Gelb and K.E. Gubbins, Langmuir **14**, 2097 (1998).
[9] J.C. Lee, Phys. Rev. B **46**, 8648 (1992).
[10] E. Pitard, M.L. Rosinberg, G. Stell, and G. Tarjus, Phys. Rev. Lett. **74**, 4361 (1995).

[11] E. Kierlik, M.L. Rosinberg, and G. Tarjus, J. Stat. Phys. **89**, 215 (1997).
[12] M. Schwartz, J. Villain, Y. Shapir, and T. Nattermann, Phys. Rev. B **48**, 3095 (1993).
[13] J.W. Cahn, J. Chem. Phys. **42**, 93 (1965).
[14] H.A. Makse, S. Havlin, M. Schwartz, and H.E. Stanley, Phys. Rev. E **53**, 5445 (1996).
[15] H.A. Makse, G.W. Davies, S. Havlin, P.C. Ivanov, P.R. King, and H.E. Stanley, Phys. Rev. E **54**, 3129 (1996).
[16] P. Wiltzius, F.S. Bates, S.B. Dierker, and G.D. Wignall, Phys. Rev. A **36**, 2991 (1987).
[17] P. Levitz, G. Ehret, S.K. Sinha, and J.M. Drake, J. Chem. Phys. **95**, 6151 (1991).
[18] M. Teubner, Europhys. Lett. **14**, 403 (1991).
[19] W.H. Press, S.A. Teukolsky, W.T. Vertterling, and B.P. Flannery, *Numerical Recipes in C* (Cambridge University, New York, 1992).
[20] U. Wolff, Phys. Rev. Lett. **62**, 361 (1989).
[21] M.E.J. Newman and G.T. Barkema, *Monte Carlo Methods in Statistical Physics* (Oxford University, New York, 2001).
[22] M.F. Sykes and J.W. Essam, Phys. Rev. **133**, A310 (1964).
[23] D. Lancaster, E. Marinari, and G. Parisi, J. Phys. A **28**, 3959 (1995).
[24] R.B. Stinchcombe, in *Phase Transitions and Critical Phenomena*, edited by C. Domb and J.L. Lebowitz (Academic, New York, 1983), Vol. 7.
[25] T. MacFarland, G.T. Barkema, and J.F. Marko, Phys. Rev. B **53**, 148 (1996).
[26] M.E.J. Newman and G.T. Barkema, Phys. Rev. E **53**, 393 (1996).
[27] J. Machta, M.E.J. Newman, and L.B. Chayes, Phys. Rev. E **62**, 8782 (2000).
[28] K.H. Fischer and J.A. Hertz, *Spin Glasses* (Cambridge University, New York, 1991).
[29] E. Marinari and G. Parisi, Europhys. Lett. **19**, 451 (1992).
[30] A.J. Liu and M.E. Fisher, Physica A **156**, 35 (1989).
[31] G.M. Torrie and J.P. Valleau, Chem. Phys. Lett. **28**, 578 (1974).
[32] D. Chandler, *Introduction to Modern Statistical Mechanics* (Oxford University, New York, 1987).
[33] J.C. Lee, Phys. Rev. Lett. **70**, 3599 (1993).
[34] B. Strickland, G. Leptoukh, and C. Roland, J. Phys. A **28**, L403 (1995).
[35] A. Chakrabarti, Phys. Rev. Lett. **69**, 1548 (1992).
[36] P.C. Hohenberg and B.I. Halperin, Rev. Mod. Phys. **49**, 435 (1977).
[37] D.S. Fisher, Phys. Rev. Lett. **56**, 416 (1986).
[38] D.A. Huse, Phys. Rev. B **36**, 5383 (1987).
[39] S.B. Dierker and P. Wiltzius, Phys. Rev. Lett. **58**, 1865 (1987).
[40] D.H. Everett, in *The Solid Gas Interface*, edited by E.A. Flood (Academic, New York, 1982), Vol. 2, p. 1055.
[41] L. Sarkisov and P.A. Monson, Langmuir **16**, 9857 (2000).
[42] A. Luzar and K. Leung, J. Chem. Phys. **113**, 5836 (2000).
[43] L.D. Landau and E.M. Lifshitz, *Fluid Mechanics* (Butterworth-Heinemann, Oxford, 1987).
[44] J.-P. Hansen and I.R. McDonald, *Theory of Simple Liquids* (Academic Press, San Diego, CA, 1986).
[45] G. Parisi, *Statistical Field Theory* (Perseus, Reading, MA, 1998).
[46] W.M. Deen, *Analysis of Transport Phenomena* (Oxford, New York, 1998).